This document is the unedited Author's version of a submitted work that was subsequently accepted for publication in Journal of Materials Chemistry A of Royal Society of Chemistry after peer review. To access the final edited and published work see: DOI: 10.1039/C7TA01114H.

Ultra-Small Carbon Nanospheres (< 50 nm) of Uniform Tunable Sizes by a Convenient Catalytic Emulsion Polymerization Strategy: Superior Supercapacitive and Sorption Performances

Received 00th January 20xx,
Accepted 00th January 20xx

DOI: 10.1039/x0xx00000x

www.rsc.org/

Vimal K. Tiwari,[a] Zhe Chen,[a] Fan Gao,[b] Zhiyong Gu,[b] Xueliang Sun,[c] and Zhibin Ye [a,*]

Porous carbon nanospheres have received enormous attention for various applications. Though there are several elegant strategies existing for the synthesis of relatively large carbon nanospheres (> ca. 100 nm), the synthesis of carbon nanospheres with well-defined tunable ultra-small sizes (< 50 nm) has often been challenging while such ultra-small nanospheres are much more valuable. A novel, convenient, and scalable catalytic emulsion polymerization technique is demonstrated in this paper for highly efficient synthesis of ultra-small carbon nanospheres with uniform tunable sizes in the range of 11–38 nm. In this strategy, a simple change of the emulsion polymerization recipe renders a convenient yet efficient tuning of the size of the carbon nanospheres. In particular, activated carbon nanospheres (A-CNS21 of average size of 21 nm) obtained by carbonization in the presence of KOH as the chemical activation agent is featured with very high surface area (2,360 m^2/g) and the desired hierarchical macro-/meso-/micropore structures resulting from nanosphere packing/aggregation. A-CNS21 is demonstrated to have superior high-rate supercapacitive performances and outstanding sorption capacities towards volatile organic compounds (VOCs), H_2, and CO_2, which are comparable to or even better than the best results reported to date in these applications. To the best of our knowledge, this is the first synthesis of ultra-small carbon nanospheres with uniform tunable sizes and superior performances for these applications by the emulsion polymerization strategy.

Introduction

Porous carbon nanospheres (CNSs) have recently received enormous attention for applications in energy storage (such as electrical double layer capacitors (EDLCs)), gas storage, organic vapor capture, and catalysis.[1] In general, porous CNSs are noted for greater pore accessibility and faster diffusions of ions/reactants, which are often the common performance parameters required in these applications. Because of the small sizes, CNSs tend to aggregate randomly, during their preparation, to conveniently form the desired 3-dimentional hierarchical pore structures that are featured with high pore volume and abundant inter-sphere macropores (> 50 nm) and/or mesopores (2–50 nm) besides the intra-sphere micropores (< 2 nm).[1,2] Therein, intra-sphere micropores contribute to the predominant energy or gas storage capacity,[3,4] while the hierarchical 3-dimensionally interconnected macropores and mesopores can serve as buffer reservoirs of ions/molecules and facilitate their fast convenient transportation into the micropores.[1,2]

Recent research in the field of carbon nanospheres has been focused on the development of synthetic strategies that facilitate the tailored design and synthesis of porous CNSs of high monodispersity, controllable size, high porosity and desirable pore size distribution, high surface area, and other structural/composition parameters to meet the application-specific requirements.[1] In this regard, various elegant synthetic strategies have been successfully developed.[1] Some most notable ones include hard templating,[5] organic-organic self-assembly (or soft templating),[6] the extended Stöber method,[7] hydrothermal carbonization,[8] and emulsion polymerization.[9] In particular, the former four have been most extensively developed in the literature, but with the carbon precursors narrowly restricted to either thermosetting polymers (mainly phenolics resins) in the former three or biomass derivatives (such as sugars) in the hydrothermal method. Emulsion polymerization is the versatile, most popular, scalable method for producing monodiperse polymer spheres of well controllable sizes (such as cross-linked polystyrene spheres).[1a] However, except in very few cases incorporating additional special post-synthesis Friedel–Crafts hyper-cross-linking,[9] it has limited use for the synthesis of porous CNSs due to structural collapse during carbonization and low carbonization yield resulting from insufficient polymer cross-linking.[9d,e]

In general, CNSs with uniform diameters in the range of ca. 100 nm to micrometers have been extensively synthesized with the above strategies.[1,5-9] However, the synthesis of ultra-small CNSs with uniform, precisely tunable diameters below ca. 50 nm (i.e., 10–50 nm) has often been challenging, while such an ultra-small size range is particularly desired for the applications. In EDLC applications, the use of ultra-small CNSs has the advantage in offering short-range intra-sphere micropores, and thus reduced diffusion paths for the ions/molecules in the micropores and better-maintained capacitance retention at high rates.[10,11]

Thus far, ultra-small CNSs with the size within 10–50 nm have only been synthesized in very few pioneering reports as follows. In these few cases, though elegant, the ultra-small size

[a] *Bharti School of Engineering, Laurentian University, Sudbury, Ontario P3E 2C6, Canada.*
[b] *Department of Chemical Engineering, University of Massachusetts, Lowell, Massachusetts 01854, United States*
[c] *Department of Mechanical and Materials Engineering, Western University, London, Ontario N6A 5B9, Canada.*

* *Corresponding author; Email: zye@laurentian.ca*
Electronic Supplementary Information (ESI) available: See DOI: 10.1039/x0xx00000x

range (<50 nm) often represents the lowest end in the large targeted size windows and is thus not the primary focus of the syntheses. In one case, hard-templated synthesis of mesoporous carbon nanoparticles with sizes as low as 10 nm was reported with mesoporous silicas as the template for carbon precursors.[5c,e] The synthesis is, however, complicated by the massive use of the silica templates and their tedious removal. Meanwhile, the ultra-small nanoparticles had rather poorly defined morphology.[5c] Zhao et al. demonstrated an innovative low-concentration synthesis of ordered mesoporous CNSs with uniform tunable sizes within 20–140 nm by the organic-organic self-assembly strategy.[6a] Therein, the very low-concentration synthesis (reactant concentration at 10^{-7} mol L^{-1}) is a restriction. Meanwhile, the resulting CNSs were only demonstrated for biological applications, but not for energy/gas storage or vapor capture applications. Through a seeded Stöber synthetic strategy, Gan et al. synthesized CNSs with tunable sizes within 30–90 nm.[7g] But the process requires the inconvenient seed preparation and a very close monitoring of the growth of the seeds for the size control. Several reports[8d-g] showed the synthesis of CNSs with sizes as low as ca. 20–50 nm by hydrothermal treatment of sugars in the presence of various additives followed with additional carbonization. CNSs obtained therein by the hydrothermal method often show irregular nonspherical morphology, and have low surface area and porosity. In addition, Jang et al. synthesized ultra-small CNSs with the size of ca. 48 nm from polypyrrole nanospheres prepared by microemulsion polymerization.[9a-c] Those CNSs also have low surface area and pore volume, and have not demonstrated for energy storage or sorption applications. Lastly, carbon quantum dots with sizes typically below 10 nm or so have also been synthesized through various techniques.[12] But they are often restricted to fluorescence-related applications and are not within the scope of porous CNSs defined herein.

Tackling the restrictions of the existing synthetic methods for ultra-small CNSs, we report in this article a new, convenient, scalable catalytic emulsion polymerization technique for the highly efficient synthesis of a range of ultra-small CNSs of uniform tunable sizes in the specifically targeted range of 10–50 nm from all commercially available precursors. The resulting CNSs have been systematically characterized for their morphological, textural, and composition properties. Meanwhile, the applications of the CNSs as high-rate electrode materials in EDLCs, and as sorbents for the capture of volatile organic compounds (VOCs) and the storage of H_2 and CO_2 have been thoroughly investigated. Some superior performances comparable to or even better than the best results reported thus far have been successfully demonstrated. To the best of our knowledge, this is the first synthesis of ultra-small carbon nanospheres with uniform tunable sizes and superior performances for these applications via the emulsion polymerization strategy.

Experimental

Materials

1,3-Diethynylbenzene (DEB, 97%, Aldrich), palladium acetate ($Pd(OAc)_2$, 98%, Strem Chemicals), α,α′-bis(di-t-butylphosphino)-o-xylene (97%, Strem Chemicals), methanesulfonic acid (99.5%, Aldrich), dichloromethane (HPLC grade, Fisher Scientific), methanol (ACS reagent, Fisher Scientific), sodium dodecyl sulphate (SDS, ≥99%, Aldrich), sulfuric acid (96%, Aldrich), titanium foil (99.95%, Aldrich), and conducting carbon (acetylene black 100%, Soltex) were all used as received. Deionized water was obtained from a Barnstead/Synbron Nanopure II water purification system.

Synthesis of polymer nanospheres (PNSs) by catalytic emulsion polymerization

The following is the typical procedure for the synthesis of PNSs with the average diameter of 21 nm. DEB (1.86 g, 14.7 mmol) was added into a flask containing an aqueous solution of SDS (0.8 g in 15.6 mL of water). The mixture was sonicated for 10 min and then stirred with a magnetic stirrer at 400 rpm for 5 h at 60 °C. A Pd catalyst solution was prepared by dissolving $Pd(OAc)_2$ (3.31 mg, 14.7 μmol) and α, α′-bis(di-t-butylphosphino)-o-xylene (17.45 mg, 44 μmol) in a mixture of dichloromethane (0.18 mL) and methanol (0.02 mL). The catalyst solution was injected into the monomer emulsion, followed with the addition of two drops of methanesulfonic acid, to start the emulsion polymerization. The polymerization lasted overnight with a maintained stirring speed of 400 rpm at 60 °C, rendering an intense dark brown emulsion dispersion. As per dynamic light scattering (DLS) analysis of the diluted dispersions, the resulting PNSs have the average size of 21 nm.

For the synthesis of PNSs with average diameter of 11 nm, DEB (0.93 g, 7.37 mmol) was added into an aqueous solution of SDS (1.0 g in 39 mL of water). The mixture was sonicated and then stirred at 60 °C. A catalyst solution, containing $Pd(OAc)_2$ (16.55 mg, 73.7 μmol) and α,α′-bis(di-*t*-butylphosphino)-*o*-xylene (87.25 mg, 221 μmol) in 0.9 mL of dichloromethane and 0.1 mL of methanol, was injected into the monomer emulsion, followed with the addition of four drops of methanesulfonic acid, to start the polymerization. The emulsion polymerization lasted overnight under stirring at 400 rpm at 60 °C. DLS analysis of the diluted emulsion showed that the resulting PNSs have the average size of 11 nm.

For the synthesis of PNSs with average diameter of 38 nm, DEB (1.86 g, 14.7 mmol) was added into an aqueous solution of SDS (0.1 g in 3.9 mL of water) in a flask, followed with sonciation and mechanical stirring at 60 °C. A catalyst solution, containing $Pd(OAc)_2$ (3.3 mg, 15 μmol) and α,α′-bis(di-*t*-butylphosphino)-*o*-xylene (17.4 mg, 44 μmol) in 0.18 mL of dichloromethane and 0.02 mL of methane, was injected into the monomer emulsion, along with the addition of one drop of methanesulfonic acid. The polymerization lasted overnight at 60 °C under the maintained stirring at 400 rpm, rendering the emulsion product.

Synthesis of carbon nanospheres by carbonization of polymer nanospheres without or with activation

The PNS emulsions prepared above were first hydrothermally treated at ca. 220 °C for overnight in a Teflon-lined autoclave. The resulting polymer precipitates were collected by filtration,

washed with an excessive amount of water, and then dried at 60 °C under vacuum for 24 h, rendering the hydrothermally treated PNSs (PNS11, PNS21, and PNS38). Direct carbonization of the hydrothermally treated PNSs without activation was performed by their pyrolysis at 800 °C for 1 h (preceded with heating at 10 °C/min from 25 to 800 °C) in a nitrogen atmosphere in a tube furnace, rendering the non-activated CNSs (CNS11, CNS21, and CNS38, respectively).

For the preparation of KOH-activated carbon nanospheres (A-CNS21), PNS21 and KOH (at 1: 3 mass ratio) were mixed in methanol, followed with the evaporation of methanol under vacuum. Carbonization was then performed using the same procedure as described above in a nitrogen atmosphere. To removal residual KOH, the carbonization product was sequentially washed with a large amount of 2% aqueous HCl solution, deionized water, and methanol. It was then dried overnight at 60 °C under vacuum, rendering the chemically activated carbon nanospheres, A-CNS21.

Characterization and Measurements

DLS measurements of the diluted emulsions (concentration at ca. 0.2 mg/mL) for sizing of the polymer nanospheres were performed on a Malvern Zeta-Sizer Nano S90 instrument at 30 °C. Transmission electron microscopy (TEM) images of the various polymer and carbon nanospheres were captured on a Philips EM400 transmission electron microscope operated at 100 keV. TEM samples were prepared by depositing a few drops of the sonicated dilute dispersion of polymer/carbon nanosphere samples in acetone (ca. 0.1 mg/mL) on lacey grids (EMS Supplies), followed with drying. For each sample, about 100 nanospheres were randomly picked and analyzed to determine the average nanosphere size and size distribution. Scanning electron microscopy (SEM) images were taken with a JEOL JSM-7401F field-emission scanning electron microscope. The samples were prepared by depositing a few drops of dilute dispersions on a small piece of conductive silicon wafer followed with drying at ambient temperature, which was then mounted to a SEM specimen stub. X-ray diffraction (XRD) patterns of the carbon samples were recorded on an X'Pert Pro diffractometer with Co radiation (wavelength 1.79 Å) at room temperature. X-ray photoelectron spectroscopy (XPS) measurements of the carbon samples were carried out on a Thermo Scientific Theta Probe XPS spectrometer. A monochromatic Al Kα x-ray source was used, with a spot area of 400 μm. Raman spectra were collected on a Renishaw InVia Raman Spectrometer, using a 514 nm laser as the excitation source.

N_2 sorption measurements of the various samples at –196 °C were carried out on a Micromeritics ASAP2020 physiosorption analyzer to determine Brunauer-Emmert-Teller (BET) specific surface area, pore volume, and pore size distribution. Before the measurements, the samples were degassed for at least 24 h at 100 and 300 °C for the polymer and carbon samples, respectively. The micropore size distribution was calculated from the N_2 sorption data within the relative pressure (P/P_0) range of 0–0.01 with the use of non-local density functional theory (NLDFT) model. The pore size distribution for pores greater than 20 Å (i.e., mesopores and macropores) was calculated from N_2 desorption data (P/P_0 = *ca.* 0.4–0.99) using the NLDFT model. The sorption isotherms of CO_2 and H_2 with the CNS samples were measured with the same instrument at 0 and –196 °C, respectively. Prior to the measurements, the carbon samples were degassed under vacuum at 300 °C for ca. 20 h.

The vapor sorption isotherms of toluene and methanol were obtained using a Belsorp-max instrument (MicrotracBel Corp.) at 25 °C. Prior to the adsorption measurement, the adsorbents (30–50 mg) were degassed under vacuum at 300 °C for ca. 20 h. The isotherms were measured from ca. 0.01 kPa up to the saturation vapor pressure of the adsorbate at 25 °C.

EDLC supercapacitor electrode fabrication and electrochemical measurement

All electrochemical measurements of the EDLC supercapacitors, including cyclic voltametry (CV), galvanostatic charge/discharge (GCD), and electrochemical impedance spectroscopy (EIS), were conducted on a Metrohm Autolab PGSTAT 100 potentiostat/galvanostat in the 2-electrode configuration with aqueous 1 M H_2SO_4 solution as the electrolyte. The electrodes were fabricated with the various carbon samples on a titanium foil (4 cm^2) as the current collector. To prepare electrodes, the active carbon sample (80 wt%), conducting carbon (10 wt%), and Nafion (10 wt%) were dispersed in ethanol under sonication in a small vial. The dispersion was then evenly coated onto the titanium current collector (active material density of 1.1 mg/cm^2). Subsequently, the electrodes were dried in an oven. Symmetrical two-electrode cells were prepared by sandwiching a piece of filtration paper between the two electrodes and were filled with the electrolyte solution. CV measurements were performed in the voltage range of 0–1 V at the voltage sweep rate of 200, 50, 25, 10, 5, 1 mV/s, respectively. The specific capacitance (C_{sp} in F/g) was calculated from the CV curves through the following equation:

$$C_{sp} = \frac{\int i dV}{m \Delta V v} \quad (1)$$

where *i* and *V* are the current and voltage, respectively, in the CV curves, *m* is the mass of the active carbon in one single electrode, and *v* is the voltage sweep rate. GCD measurements were performed within voltage range of 0–1 V at current densities of 50, 30, 20, 10, 5, 3, 2, 1, 0.5, 0.25, and 0.1 A/g, respectively. C_{sp} was also calculated from the discharge curve through the following equation:

$$C_{sp} = \frac{2i}{m dV/} \quad (2)$$

where *i* is the discharge current, *m* is carbon mass in each electrode, and d*V*/d*t* is calculated as the slope of the discharge curve within the voltage range following the end of ohmic drop to the end of the discharge curve. The energy density (*E*, in Wh/kg) and power density (*P*, W/kg) were calculated according to:

$$E = \frac{1}{2} C_{sp} V^2 \cdot \frac{1}{4} \cdot \frac{1}{3.6} \quad (3)$$

$$P = \frac{E}{t} \quad (4)$$

where V is the cell voltage after ohmic drop and t is the discharge time (in h). The EIS measurement was also conducted at static potential of 0 V over the frequency range from 10 kHz to 0.01 Hz with an AC perturbation of 10 mV.

Results and discussion

Synthesis and Characterization of Carbon Nanospheres by Catalytic Emulsion Polymerization

The synthesis of ultra-small CNSs herein involves three steps: (1) catalytic emulsion polymerization of 1,3-diethynylbenzene (DEB), (2) simple hydrothermal treatment of resulting polymer nanospheres, and (3) carbonization of the polymer nanospheres. It involves the exclusive use of commercially available precursors. Scheme 1 illustrates schematically the synthetic procedure. Unique in this strategy, DEB, a difunctional cross-linkable alkyne monomer (molecular formula C_8H_6) featured with a high carbon content (95 wt%), is employed as the monomer precursor for the catalytic emulsion polymerization. This differs from the traditional synthesis of CNSs by emulsion polymerization, where styrenics (divinylbenzene and styrene with the former as the cross-linker) are commonly employed for the emulsion synthesis of cross-linked styrenic PNSs via the radical mechanism.[9d,e] However, styrenic PNSs often undergo severe structural collapse during carbonization, along with low carbon yield, due to limited cross-linking density.[9d,e] On the contrary, we have shown in our recent work that Pd-catalyzed coordinative addition polymerization of DEB can efficiently yield non-nanostructured highly cross-linked polymers, which can subsequently give rise to porous carbons with particle sizes in the micrometer range at high yield (83%) by simple pyrolysis.[13] The desirable feature triggers us to develop ultra-small carbon nanospheres from poly(DEB) nanospheres produced from DEB as the monomer precursor by emulsion polymerization.

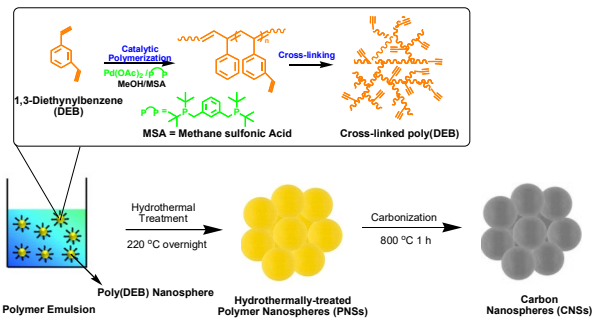

Scheme 1. Schematic synthesis of carbon nanospheres by catalytic emulsion polymerization of DEB.

In this method, emulsion polymerization of DEB was undertaken at 60 °C with the use of an in situ generated cationic diphosphine-ligated Pd catalyst, $Pd(OAc)_2/\alpha,\alpha'$-bis(di-tert-butylphosphino)-o-xylene/methanesulfonic acid.[14] Due to its low oxophilicity, the catalyst is extremely active despite in the polar aqueous media,[15] requiring only a very low Pd loading ([Pd]/[DEB] ratio (as low as 1/3000). SDS is used as the surfactant with its concentration in the range of 0.025–0.05 g/mL, which is far greater than its critical micelle concentration of ca. 0.0029 g/mL so as to achieve miniemulsions.[16] In this emulsion polymerization system, the micelles, that contains DEB, acts as nano-scale reactors, rendering poly(DEB) PNSs. For this system, we have found that a change in SDS concentration in the above range shows no pronounced effects on the size of the resulting PNSs. Instead, the feed concentration of DEB monomer in water has the predominant effect on the size of the PNSs. Efficient tuning of the size of PNSs can be conveniently achieved by simply changing the DEB feed concentration in water. As a demonstration, a range of PNSs having three different average sizes (PNS11, PNS21, PNS38 with the average diameter of 11, 21, and 38 nm, respectively determined by DLS and/or TEM characterizations) were synthesized at different DEB concentrations, 0.024, 0.12, and 0.48 g/mL, respectively. This range of monomer feed concentrations is about an order of magnitude higher than those used in the low-concentration synthesis of ultra-small mesoporous CNSs by Zhao et al.,[6a] indicating the significantly enhanced productivity herein. Particle size analysis of the three as-produced PNS miniemulsions by both DLS and TEM confirms their average sizes and the very narrow size distribution (polydispersity index as low as 0.02 and 0.08 for PNS11 and PNS21, respectively, as per DLS; see Figure S1 in ESI).

The resulting emulsions containing PNSs were subsequently treated hydrothermally at ca. 220 °C. We have found that the hydrothermal treatment renders the resulting CNSs with better-retained nanosphere morphology during the subsequent carbonization, which is attributed to the further enhanced cross-linking density within the PNSs by continued polymerization reactions at the elevated temperature during the hydrothermal treatment. Meanwhile, the treatment also decomposes/destabilizes SDS and facilitates its easy removal through simple washing, which is otherwise difficult to remove from the as-produced emulsions even by extensive washing. From the weights of hydrothermally treated PNSs, DEB conversion during the emulsion polymerizations was found to be nearly quantitative (over 90% in all cases). The hydrothermally treated PNSs were then carbonized at 800 °C for 1 h under the N_2 atmosphere in the absence of any activation agent to render the CNSs (CNS11, CNS21, and CNS38, respectively, with the number representing the average size of the CNSs). Relative to the PNS precursors, the yield of CNSs is about 80 wt%, which is very high relative to many other polymer precursors.[13] This confirms the very high atomic efficiency for the conversion of poly(DEB) to carbon.

Figure 1 shows TEM images of the hydrothermally treated PNSs and their resulting CNSs. Figure S2 in ESI shows the SEM images of PNS21 and CNS21 as representative samples. All the PNS and CNS samples are composed of aggregates/compacts of well-defined nanospheres of very uniform sizes. Commonly observed with various carbon nanospheres, such packing/aggregation is highly desirable, generating the valuable hierarchical macro-/meso-/micropore structures in the carbon materials that facilitate their applications as superior high-rate electrode materials and fast-adsorbing sorbents. In the case of PNS11 and CNS11, aggregation of the nanospheres is more severe compared to the others with a fraction of fused nanospheres observed in CNS11, which is expected due to their smallest nanosphere sizes. By analyzing more than 100 nanospheres from the TEM images of each sample, the average size of the PNS samples agrees well with those determined by DLS analysis of the as-produced emulsions, indicating that the hydrothermal treatment has no pronounced effect on the size of the polymer nanospheres. Meanwhile, the resulting CNSs also have nearly identical average nanosphere size as the corresponding PNS precursors with no obvious deterioration in the nanosphere morphology during the carbonization. The TEM and SEM images confirm solidly the successful synthesis of the CNSs of well-defined easily tunable ultra-small sizes in the desired range of 11–38 nm by this catalytic emulsion polymerization strategy.

N_2 sorption characterization of the CNS samples (CNS11, CNS21, and CNS38), as well as PNS21 as a representative PNS sample, was undertaken at –196 °C. Figure 2(a) shows the N_2 sorption isotherms of the samples, with the results summarized in Table 1. Generally, the samples (CNS samples and PNS21) all show typical type IV isotherms,[17] with a slight uptake in the low relative pressure range ($P/P_0 < 0.1$), a sharp uptake at the high relative pressure end ($0.8 < P/P_0 < 1$), and the presence of a distinct hysteresis loop in the P/P_0 range of 0.8–1. Except CNS11 that shows a hysteresis loop intermediate between types H1 and H3, PNS21, CNS21, and CNS38 all show a type H1 hysteresis loop,[17] with the two branches being almost vertical and parallel over an appreciable range of N_2 uptake. The type H1 hysteresis is often associated with agglomerates/compacts of approximately uniform spheres in fairly regular array.[17] This also confirms the uniform nanospheres present in these samples (PNS21, CNS21, and CNS38) and suggests their relatively regular packing to form narrow-distributed inter-nanosphere pores. On the contrary, the type H3 hysteresis loop is often observed in aggregates of plate-like particles that give rise to slit-shaped pores.[17] The intermediate hysteresis loop in CNS11 is indicative of the presence of a fraction of plate-like particles formed by fusion of nanospheres during carbonization, which is in agreement with the finding from its TEM image (Figure 1(b)).

The polymer nanospheres in PNS21 appear to be solid with negligible intra-sphere micropores given the marginal N_2 uptake at the low relative pressure range. It has a low BET surface area of 199 m^2/g, with negligible micropore surface area, and a high total pore volume of 1.80 cm^3/g arising exclusively from the inter-sphere mesopores/macropores

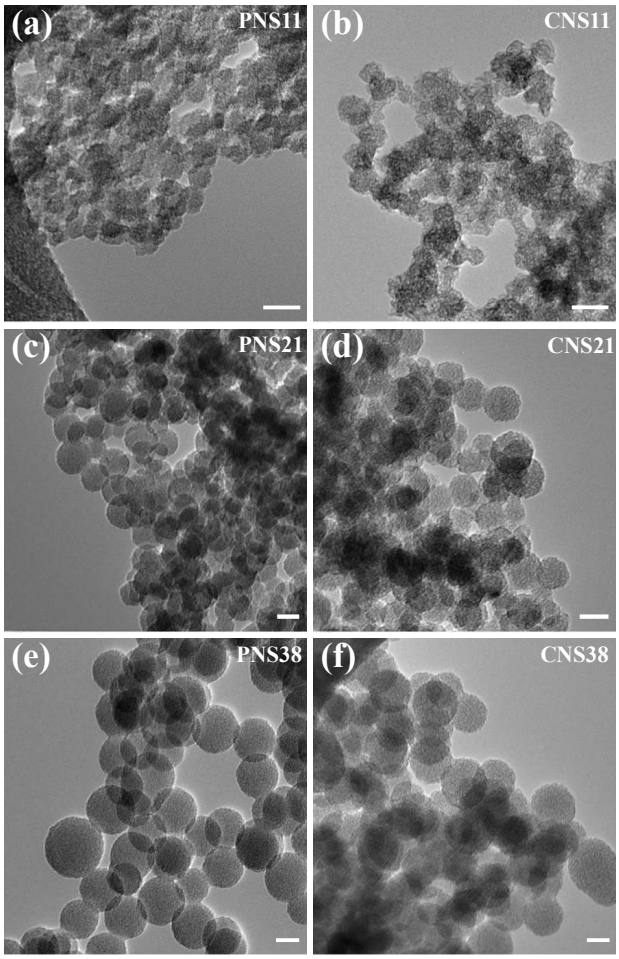

Figure 1. TEM images of the polymer nanospheres (PNS11, PNS21, and PNS38) and their corresponding carbon nanospheres (CNS11, CNS21, and CNS38) obtained by carbonization at 800 °C for 1 h. Scale bar = 20 nm.

generated by the packing/aggregation of nanospheres. The carbon nanospheres in the CNS samples (CNS11, CNS21, and CNS38) have a total BET surface area of 493, 580, and 407 m^2/g, respectively, and a total pore volume of 1.04, 1.52, and 1.13 cm^3/g, respectively (see Table 1). They have significant intra-sphere micropores, with the micropore surface area contributing about 60% of surface area in CNS21 and CNS38, and 33% in CNS11. But the majority (90%) of pore volume arises from inter-sphere mesopores/macropores generated by the packing/aggregation of the CNSs. Figure 2(b) compares the mesopore/macropore size distribution of the samples obtained with the NLDFT model. PNS21, CNS21, and CNS38 have the pore size distribution primarily in the narrow range of 40–66 nm, with similar average mesopore/macropore sizes (44.3, 41.6, and 40.7 nm, respectively). In particular, CNS21 has a similar distribution pattern as its precursor PNS21 and both have the peak distribution intensity at 63 nm. Instead, CNS11 show a broader distribution within 2–60 nm, with the peak distribution intensity at around 12 nm and a lowered average mesopore/macropore size of 26.1 nm.

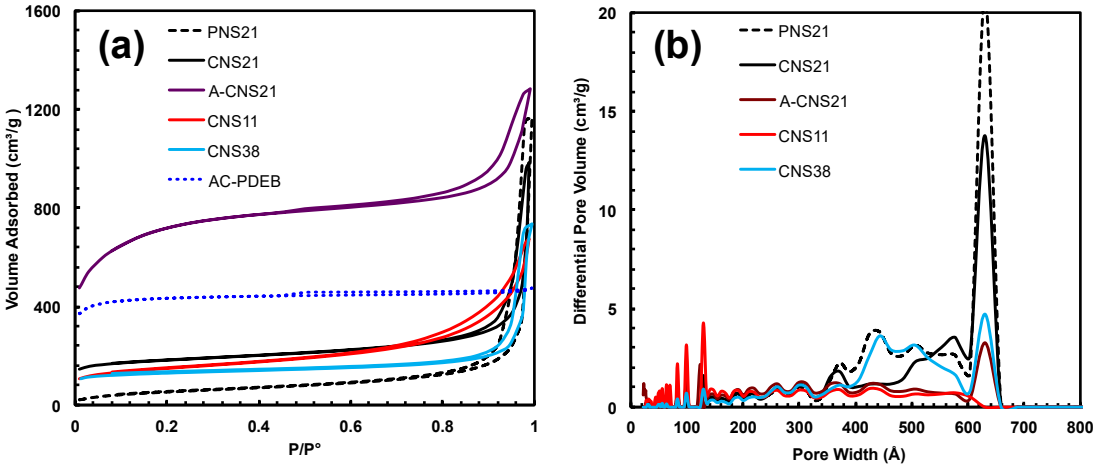

Figure 2. (a) N_2 sorption curves of various CNS and PNS samples; (b) their mesopore/macropore size distribution curves determined with the NLDFT model.

Figure S3 in ESI shows the XRD pattern of CNS21 as a representative sample. There is an intense diffraction peak with peak maximum at ca. 3.9°, indicating the presence of high-density pores within the carbon materials.[13] In addition, a broad weak peak is present at around 28°, which is attributed to the (002) peak of graphitic structures.[18-20] The weak and broad nature of the peak indicates a low degree of graphitization in the carbon material. As expected, this is typical of amorphous carbon materials prepared by pyrolysis at the relatively low temperature due to insufficient graphitization.[19] An increase of pyrolysis temperature is expected to improve their graphite content, which will be investigated in subsequent studies.

The above CNS samples produced by carbonization without activation all possess relatively low surface area and insufficient micropores. To obtain carbon nanospheres of enhanced surface area for applications as high-capacitance supercapacitor electrode materials or high-capacity sorbents, we have also prepared a KOH-activated carbon nanosphere sample, A-CNS21, by simply carbonizing PNS21 in the presence of KOH (at a KOH/PNS21 mass ratio of 3/1) as the chemical activation agent under N_2 at 800 °C for 1 h. Figure 3(a) shows a TEM image of A-CNS21. The nanosphere morphology is still clearly observable in the TEM image. Its N_2 sorption isotherm is also included in Figure 2(a). A strong uptake is seen in the low relative pressure range, indicative of the significant presence of micropores, along with a hysteresis loop intermediate between types H1 and H3 within the relative pressure range of 0.7–1. It has a high BET surface area of 2,360 m^2/g and a high total pore volume of 1.98 cm^3/g, which are dramatically enhanced relative to the non-activated CNS21. Meanwhile, it also has significant micropore size surface area (882 m^2/g; 37% of total surface area) and micropore volume (0.46 cm^3/g; 23% of total pore volume).

Table 1. Textural properties of the polymer/carbon samples determined by N_2 sorption at –196 °C.

Sample	Surface Area[a] (m^2/g)			Pore Volume[b] (cm^3/g)			Average Pore Size[c] (Å)	
	S_{BET}	S_{micro}	$S_{meso/macro}$	V_{total}	V_{micro}	$V_{meso/macro}$	$d_{meso/macro}$	d_{micro}
PNS21	199	0	199	1.80	0	1.80	443	
CNS21	580	323	256	1.52	0.17	1.35	416	7.3
CNS11	493	165	327	1.04	0.09	0.95	261	8.3
CNS38	407	249	158	1.13	0.13	1.00	407	8.0
A-CNS21	2360	882	1477	1.98	0.46	1.52	268	9.1
AC-PDEB	1308	1081	228	0.73	0.57	0.16		8.0

[a] BET surface area (S_{BET}), as well as surface area of micropores (S_{micro}) and mesopores/macropores ($S_{meso/macro}$) determined with t-plot method.

[b] Total pore volume (V_{total}), as well as micropore volume (V_{micro}) and mesopore/macropore volume ($V_{meso/macro}$) determined with t-plot method.

[c] Average micropore size (d_{micro}) and mesopore/macropore size ($d_{meso/macro}$) determined with NLDFT model.

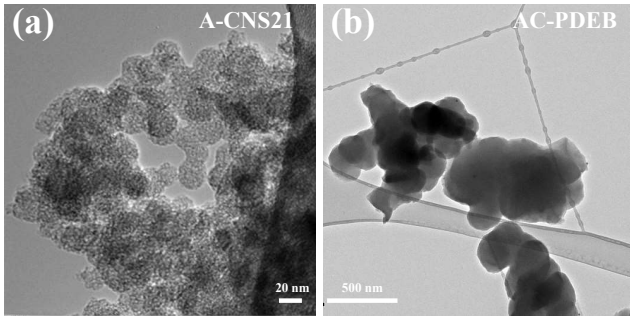

Figure 3. TEM images of (a) A-CNS21 and (b) AC-PDEB.

Clearly, the use of KOH as the activation agent is highly efficient in generating significant intra-sphere micropores and mesopores. Compared to CNS21, its average mesopore/macropore size is slightly reduced to 26.8 nm, due to the creation of small intra-sphere mesopores and narrowing of some of the inter-sphere mesopores/macropores upon activation. Nevertheless, like CNS21, A-CNS21 shows the peak distribution intensity at 63 nm in the mesopore/macropore size distribution curve (see Figure 2(b)), confirming the significant retention of nanosphere morphology despite the involvement of chemical activation. Its textural/pore structures make A-CNS21 resemble carbon aerogels prepared by sol-gel routes.[2e]

For the purpose of comparison, we have also synthesized an activated carbon control sample, AC-PDEB, from the non-nanostructured cross-linked polymer of DEB (PDEB) synthesized in our previous work[13] as the polymer precursor of the same chemical composition as PNS21. Unlike PNS21, PDEB synthesized by conventional catalytic polymerization in organic media, does not contain designed nano-structures. Under TEM, it has irregular large sizes (ca. 1–10 μm).[13] AC-PDEB was obtained by carbonization of PDEB in the presence of KOH at identical conditions as for A-CNS21. Figure 3(b) shows a TEM image of AC-PDEB, where irregular particles with dimensions in the range of around 0.2 μm to a few microns can be seen. AC-PDEB shows a type I isotherm with a negligibly small hysteresis loop (see Figure 2(a)) and is thus predominantly microporous with marginal meso-/macropore structures. This marks its distinct difference from A-CNS21 of hierarchical macro-/meso-/micropore structures synthesized from nanostructured PNSs. AC-PDEB has a BET surface area of 1,308 m^2/g and a total pore volume of 0.73 cm^3/g, with the majority (83 and 78%, respectively; see Table 1) arising from micropores. As per micropore analysis via the NLDFT model, A-CNS21 has a slightly higher average micropore size (9.1 vs. 8.0 Å) than AC-PDEB (see Figure S4 in ESI for micropore size distribution).

Both A-CNS21 and AC-PDEB were characterized with XPS for their chemical composition and chemical identity. The atomic composition survey reveals that A-CNS21 contains C at ca. 92 atom% and O at 7 atom% while AC-PDEB has the corresponding contents of 95 and 4 atom%, respectively (see Figure S5 in ESI). The slightly higher O content in A-CNS21 than in AC-PDEB should result from the inter-sphere mesopores/macropores present in PNS21, which facilitate deeper and more uniform penetration of KOH for enhanced chemical activation. Figure S6 in ESI shows the Raman spectra of PNS21, A-CNS21 and AC-PDEB. While PNS21 exhibits no Raman peak in the given region, both A-CNS21 and AC-PDEB show similar spectra with broad overlapping D and G bands centered at 1350 and 1588 cm^{-1}, respectively. The intensity ratio of D and G bands is 0.88 and 0.94 for A-CNS21 and AC-PDEB, respectively, suggesting a low degree of graphitization of the carbons.[5c]

AC-PDEB is employed as the activated carbon control sample in our subsequent study on the performances of A-CNS21 as the EDLC electrode material, and the sorbent for CO_2/H_2 storage and the capture of VOCs. We reason that AC-PDEB, synthesized from polymer precursors of identical chemical composition via the same procedure as A-CNS21, should better serve this purpose than other commercial activated carbons. Compared to AC-PDEB synthesized herein, commercial activated carbons are often obtained from complex natural precursors by different pyrolysis treatment procedures.

Electrochemical Supercapacitive Performances

With their hierarchical pore structures and ultra-small nanosphere size, high-surface-area CNSs synthesized through our catalytic emulsion polymerization strategy are reasoned to be promising superior electrode materials for EDLCs with high capacitance and capacitance retention at high currents. As a proof-of-concept demonstration, A-CNS21 has been thoroughly evaluated herein for its electrochemical supercapacitive performances in a two-electrode symmetrical cell in 1 M H_2SO_4 aqueous electrolyte. CV, GCD, and EIS measurements were undertaken, with the results summarized in Figure 4 and Figure S7 in ESI. The CV curves shown in Figure 4(a) exhibit the typical rectangular shapes even at the high voltage sweep rate of 200 mV/s, along with only small reductions in the area of the rectangles with the gradual increase of voltage sweep rate from 5 to 200 mV/s. These are indicative of the ideal capacitive behavior and the excellent capacitance retention at the high sweep rates. The specific capacitance calculated from the CV curves decreases only slightly from 214 F/g at 5 mV/s to 167 F/g at 200 mV/s, representing 78% of capacitance retention at 200 mV/s. In contrast, the CV curves of AC-PDEB (see Figure S8(a) in ESI) show increasingly obvious distortions from the rectangular shape with the increasing sweep rates, along with the pronounced decrease in the enclosed area. Its specific capacitance calculated from the CV curves shows a severe drop from 187 F/g at 5 mV/s to 101 F/g at 200 mV/s, representing only 54% of retention.

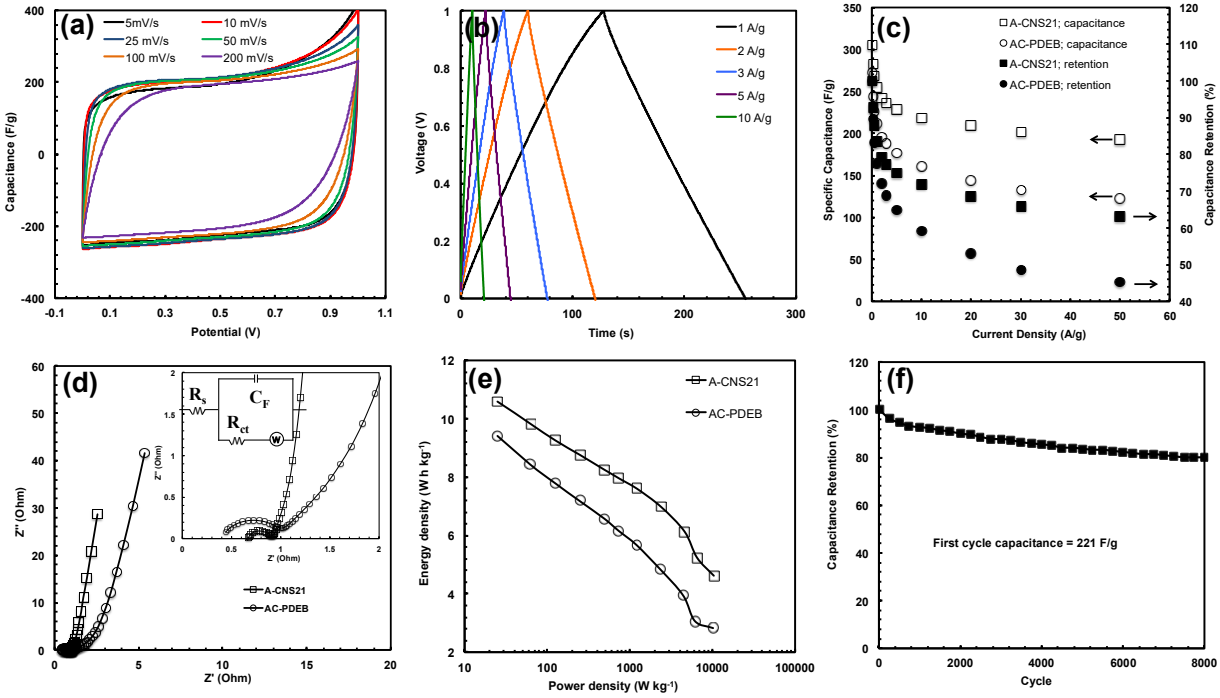

Figure 4. Electrochemical supercapacitive results of A-CNS21 in a two-electrode cell configuration in 1 M H_2SO_4 aqueous electrolyte: (a) CV curves at different voltage sweep rates; (b) GCD curves at different current densities (1–10 A/g); (c) specific capacitance and capacitance retention as functions of current density; (d) Nyquist plot with inset showing the high frequency region and electrical equivalent circuit for fitting the impedance spectra; (e) Ragone plot; (f) cyclic stability at the current density of 5 A/g over 8,000 charge-discharge cycles. The results of AC-PDEB at identical measurements conditions are included in (c)–(e) for comparison.

The GCD curves of A-CNS21 (see Figures 4(b) and S7) also exhibit the typical triangular shapes found with ideal capacitors. The voltage drops in the discharge curves resulting from equivalent series resistance are favorably small (e.g., only 0.068 V at 10 A/g). Figure 4(c) plots the specific capacitance and capacitance retention obtained from the GCD measurements at different current densities. A high specific capacitance of 305 F/g is obtained at 0.1 A/g, with only slight decreases to 255 and 219 F/g at 1 and 10 A/g, respectively. On the contrary, the specific capacitance values of AC-PDEB are 273, 211, and 160 F/g at the three corresponding current densities. Meanwhile, the percentages of capacitance retention of A-CNS21 at the various high current densities far exceed those of AC-PDEB. For example, in reference to the specific capacitance at 0.1 A/g, 72% of capacitance retention is achieved with A-CNS21 at 10 A/g while the corresponding retention is 58% for AC-PDEB. The high specific capacitance and capacitance retention values achieved herein with A-CNS21 exceed or compare well to those of many other high-performance porous carbons (see Table S1 in ESI). For example, high-performance hollow carbon nanospheres (outer diameter: 69 nm) of ultra-high surface area (3,022 m^2/g) developed elegantly by Wu et al. were reported to show specific capacitance values of 203, 180, and 153 F/g at 0.1, 1, and 10 A/g, respectively, which are appreciably lower than the values obtained herein with A-CNS21 though with similar capacitance retentions.[6i] However, unlike A-CNS21, the synthesis of hollow carbon nanospheres therein requires extremely long high-temperature carbonization (20 h) and precisely controlled temperature ramping rate, which may be challenging for applications.

Figure 4(d) compares the Nyquist plots of A-CNS21 and AC-PDEB, obtained from EIS measurements within the frequency range of 10 kHz to 0.01 Hz. The equivalent circuit for the fitting of the EIS data is included therein, where R_s is the intrinsic ohmic resistance, C_F is a double-layer capacitor, R_{ct} is the faradic charge transfer resistance, and W is the Warburg impedance. Both carbons show a distinct semicircle at high frequency and a nearly vertical line at low frequency. In the plot of AC-PDEB, an additional long inclined Warburg-type line (with a slope at about 45°; see inset in Figure 4(d)) at intermediate frequency is present while it is nearly absent in the plot of A-CNS21. It is known that the semicircle corresponding to the faradic charge-transfer resistance arises primarily from the ion transport within the mesopores and the Warburg-type line is ascribed to the ion movement within micropores.[19b] Herein, the semicircle of A-CNS21 is much smaller (0.227 Ω) than that (0.553 Ω) of AC-PDEB (see the inset in Figure 4(d)), indicating the significantly lowered ion transport resistance within mesopores in A-CNS21 due to the presence of the abundant mesopore volume within the hierarchical structures. Meanwhile, the absence of the Warburg line in A-CNS21 also confirms the dramatically reduced ion transfer resistance within its intra-sphere

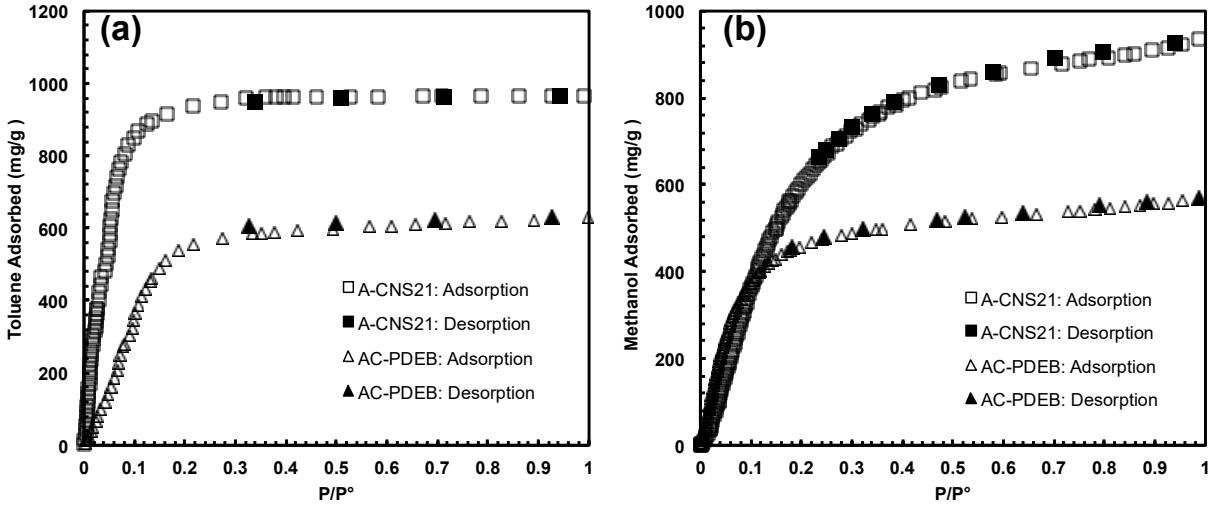

Figure 5. Sorption isotherms of A-CNS21 and AC-PDEB towards the vapor of toluene (a) and methanol (b) at 25 °C.

micropores due to their shortened diffusion length as a result of the ultra-small nanosphere size and/or the presence of intra-sphere mesopores. The intrinsic ohmic resistance (the first intercept of the semicircle along the real axis) of A-CNS21 is slightly higher than that of AC-PDEB (0.67 vs. 0.44 Ω), indicating the slightly lower conductivity in A-CNS21 due to the higher porosity. But the equivalent series resistance (ESR), obtained by extrapolating the vertical portion in the low-frequency region, is significantly lower in A-CNS21 than in AC-PDEB (1.16 vs. 2.54 Ω). The difference of 1.38 Ω in the two ESR values should result from the smaller charge transfer resistance and more importantly, the faster ion diffusion within shorter micropores in A-CNS21.

The Ragone plot (see Figure 4(e)) shows that a high energy density of 10.6 Wh/kg is achieved with A-CNS21, which is much higher than the common carbon electrode of about 5 Wh/kg.[6i] A cyclic stability test was performed on a two-electrode cell fabricated with A-CNS21 for 8,000 GCD cycles at 5 A/g. Figure 4(f) plots the capacitance retention curve. About 80% of the initial capacitance (221 F/g) is retained after 8,000 cycles, confirming its excellent cyclic stability.

VOC Sorption Performances

With its high surface area and pore volume, A-CNS21 of hierarchical pore structures is also highly attractive for adsorption of VOCs that are of serious environmental concern. Herein, its adsorption properties towards the vapor of two representative VOCs, toluene and methanol, have been investigated, along with AC-PDEB for comparison. Figure 5 shows the adsorption isotherms measured at 25 °C, with the adsorption capacity at different relative vapor pressures (P/P_0) summarized in Table 2. From the figure, both A-CNS21 and AC-PDEB exhibit type I isotherms for the adsorption of both toluene and methanol vapors. A-CNS21 shows the maximum adsorption capacities of 967 and 937 mg/g for toluene and methanol, respectively, at P/P_0 of 0.99. These maximum capacity data are very high and are well comparable to those of many other porous materials studied for organic vapor adsorption (see Table S2 in ESI), such as porous carbons (456–1,500 mg/g and 243–1,230 mg/g for toluene and methanol, respectively), microporous polymers (780–1,357 mg/g and 289–934 mg/g for toluene and methanol, respectively), and metal organic framework (MOF, 125–1,285 mg/g and 100–480 mg/g for toluene and methanol, respectively).[6i] Among the various porous carbons reported for the adsorption of toluene and methanol vapors, the maximum adsorption capacity data achieved with A-CNS21 herein are the second highest, only lower than those (1,500 and 1,230 mg/g for toluene and methanol, respectively) reported for hollow carbon nanospheres of ultra-high surface area developed by Wu et al.[6i]

Most distinctively, A-CNS21 shows extremely high adsorption capacity for both toluene and methanol within the low P/P_0 range ($P/P_0 < 0.1$), with very steep isotherms. At P/P_0 of 0.01, it has the adsorption capacities of 159 and 21 mg/g towards toluene and methanol, respectively. At P/P_0 of 0.05, the capacities are 585 and 167 mg/g for toluene and methanol, respectively. With the further increase of P/P_0 to 0.1, the values reach 866 and 366 mg/g for toluene and methanol, respectively. These data suggest the highly responsive capture of the VOCs at the low P/P_0 range. Beyond this range (i.e., $P/P_0 > 0.1$), the toluene adsorption capacity (951 mg/g) is almost saturated at P/P_0 of 0.27, with marginal increase afterwards. While for methanol, the adsorption capacity still shows continuous increase though at reduced rates with the further increase of P/P_0.

The excellent adsorption capacities of A-CNS21 towards toluene and methanol vapors at low P/P_0 (<0.1) are even better than those of various types of high-performance

Table 2. Vapor and gas adsorption capacity data.

Sample	Methanol adsorption capacity (in mg/g) at different P/P_0[a]				Toluene adsorption capacity (in mg/g) at different P/P_0[a]				CO_2 adsorption capacity[b] (wt%)	H_2 adsorption capacity[c] (wt%)
	P/P_0= 0.01	P/P_0= 0.05	P/P_0= 0.1	P/P_0= 0.99	P/P_0= 0.01	P/P_0= 0.05	P/P_0= 0.1	P/P_0= 0.99		
A-CNS21	21	167	366	937	159	585	866	967	26	2.5
AC-PDEB	46	250	380	572	38	163	366	631	28	2.4

[a] Methanol and toluene adsorption capacity measured at 25 °C.
[b] CO_2 sorption capacity measured at 0 °C and 1 bar.
[c] H_2 sorption capacity measured at –196 °C and 1 bar.

sorbents featured with higher maximum adsorption capacities (see Table S2). For example, though showing strikingly high maximum adsorption capacities, the hollow carbon nanospheres developed by Wu et al. show the adsorption capacities of ca. 800 and 240 mg/g for toluene and methanol, respectively, at P/P_0 of 0.1,[6i] which are lower than the corresponding values (866 and 366 mg/g for toluene and methanol, respectively) of A-CNS21. For another instance, a mesoporous aromatic framework showed a toluene adsorption capacity of ca. 800 mg/g at P/P_0 of 0.1 though having an excellent maximum adsorption capacity of 1,355 mg/g toward the saturated toluene vapor.[21] Compared to a well-known MOF, HKUST-1 with a remarkable toluene adsorption capacity of ca. 608 mg/g at low P/P_0 of 0.06,[22] the adsorption capacity of A-CNS21 at the same condition (697 mg/g) is also higher, along with a higher maximum capacity (967 vs. 620 mg/g). These remarkable adsorption performance properties of A-CNS21 should result from its valuable textural properties, including the high surface area and the rich presence of micropores with matching sizes for efficient adsorption of both toluene and methanol molecules. These performance properties make A-CNS21 a most suitable adsorbent for the adsorption of toluene and methanol at very low concentrations, suggesting its promising use in controlling indoor air contamination of VOCs.

Compared to A-CNS21, AC-PDEB has much lowered maximum adsorption capacities for both toluene and methanol (631 and 572 mg/g, respectively), which should result from its significantly lower total surface area. In the low P/P_0 range (P/P_0 < 0.1), AC-PDEB, however, shows slightly higher methanol adsorption capacity than AC-CNS21 while the opposite is found in the toluene adsorption. This is reasoned to result from the slightly smaller average micropore size in AC-PDEB, which better matches the adsorption of methanol molecules of a smaller size.

CO_2 and H_2 Adsorption Performances

A-CNS21 has also been evaluated for its performances as the sorbent for the adsorption of CO_2 at 0 °C and H_2 at –196 °C. Figure 6 shows its adsorption isotherm within the pressure range of 0–1 bar at the respective temperatures, along with those of AC-PDEB for comparison. For both CO_2 and H_2, the desorption isotherms have been found to overlap well with the corresponding adsorption isotherms with the absence of hysteresis, confirming the reversible adsorption and desorption. The adsorption capacity data at 1 bar are summarized in Table 2. At 0 °C and 1 bar, A-CNS21 has a CO_2 adsorption capacity of 26 wt% or 5.8 mmol/g and AC-PDEB has a slightly higher capacity of 28 wt% or 6.4 mmol/g. In CO_2 capture from flue gas, the selectivity of the sorbents towards CO_2 relative to other species such as N_2 is also critically important besides the adsorption capacity. The N_2 adsorption isotherm of A-CNS21 is also included in Figure 6(a), which shows significantly reduced adsorption across the whole relative pressure range. The CO_2/N_2 Henry selectivity of A-CNS21 is determined to be 10.8, which is high for pure carbon-based sorbents.[13] A similar selectivity value of 11 is found for AC-PDEB.[13]

Among various sorbents, porous carbons are most promising for CO_2 capture with easy low-cost synthesis, resistance to water, and higher adsorption capacities under ambient conditions. At 0 °C and 1 bar, the CO_2 adsorption capacities of porous carbons are generally in the range of 11–39 wt% (see Table S3 in ESI), with a predominant dependence on small micropores with sizes below 0.8 nm.[4d-f] A very high CO_2 adsorption capacity of 38 wt% was reported by Silvestre-Albero et al. for a microporous activated carbon obtained from petroleum pitch precursors (BET surface area, 2450 m^2/g; total pore volume, 1.12 cm^3/g; micropore volume, 1.03 cm^3/g).[23] But it was featured with a very low CO_2/N_2 selectivity of 2.8. The highest adsorption capacity of 39 wt% for porous carbons is reported by Jaroniec and Wickramaratne with KOH-activated phenolic resin-based carbon spheres,[4f] but with no information given on the selectivity.

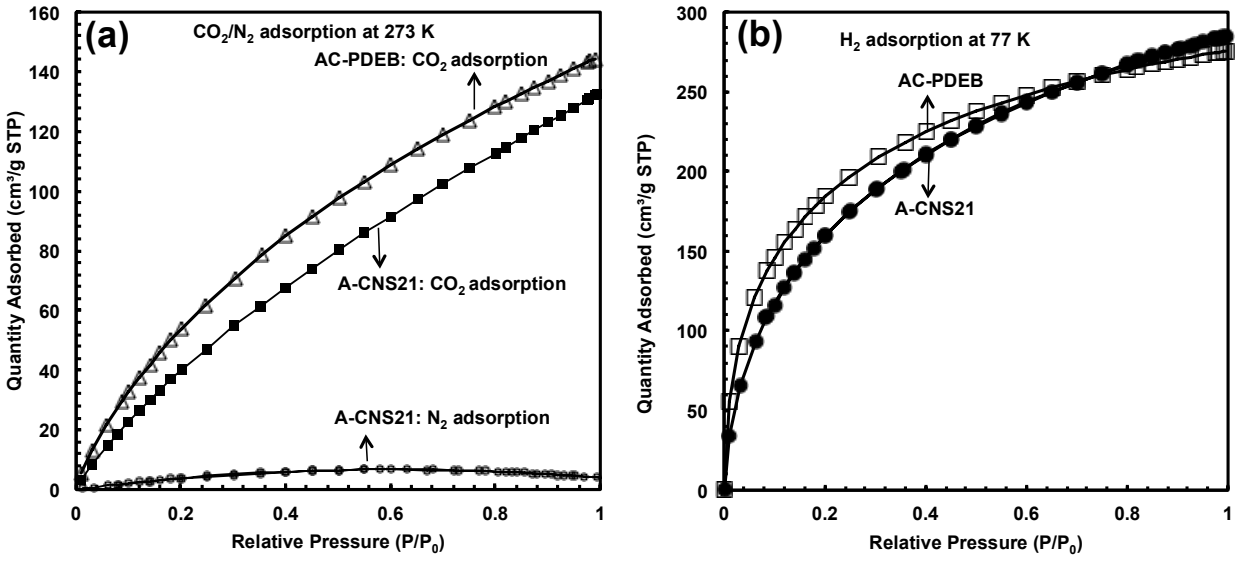

Figure 6. (a) CO_2/N_2 adsorption isotherms at 0 °C of A-CNS21 and AC-PDEB; (b) their H_2 adsorption isotherms at –196 °C.

The CO_2 adsorption capacities achieved herein with both A-CNS21 and AC-PDEB are high relative to those achieved with many other porous carbons, though not highest. In particular, their overall performances are promising in view of their high CO_2/N_2 selectivity. Compared to A-CNS21, the slightly higher capacity found with AC-PDEB should result from its slightly higher volume/surface area of micropores less than 0.8 nm (0.35 m^3/g and 903 m^2/g vs. 0.27 cm^3/g and 741 m^2/g).

A-CNS21 has a H_2 adsorption capacity of 2.5 wt% at 1 bar and –196 °C, with a very similar capacity value of 2.4 wt% found for AC-PDEB. For nanoporous carbons, the H_2 adsorption capacity shows the predominant dependence on small micropores with sizes below 1.0 nm.[4a,b] Herein, the two samples have the similar volume and surface area of micropores less than 1.0 nm, with the values of A-CNS21 being slightly higher (0.51 cm^3/g and 1,205 m^2/g for A-CNS21; 0.41 cm^3/g and 1,035 m^2/g for AC-PDEB). Though not highest, these capacity data are well comparable to those (0.2–3.25 wt%) reported in the literature for various porous carbons (see Table S4 in ESI). To the best of our knowledge, the highest H_2 storage capacity reported for porous carbons at 1 bar and –196 °C is 3.25 wt% with a MOF-derived primarily microporous carbon with exceptionally high surface area (3,447 m^2/g) and pore volume (1.45 cm^3/g).[24]

While no dramatic improvements are found herein with A-CNS21 in comparison to AC-PDEB in terms of the CO_2/H_2 adsorption capacities due to their primary dependences on small micropores, we reason that the adsorption kinetics can be improved with A-CNS21 under circumstances where the diffusion of the adsorbate molecules in the micropores is an issue, such as in viscous systems. The hierarchical pore structures with abundant large meso-/macropores in A-CNS21 may offer faster diffusion of adsorbate molecules into micropores and thus offer the advantage of improved adsorption kinetics in those cases. This is to be further investigated in our subsequent studies.

Conclusions

A new catalytic emulsion polymerization strategy employing DEB as the monomer precursor has been successfully demonstrated for the efficient synthesis of ultra-small carbon nanospheres of uniform tunable sizes (11–38 nm) in a gram scale. By simply changing the DEB feed concentration in the emulsion polymerization, polymer nanospheres (PNS11, PNS21, and PNS38) of uniform tunable sizes have been conveniently obtained with high monomer conversion. Carbonization of the PNSs after hydrothermal treatment without activation gives rise to the corresponding carbon nanospheres (CNS11, CNS21, and CNS38) of well-retained nanosphere morphology and sizes. Carbonization of PNS21 in the presence of KOH renders effectively A-CNS21 of very high surface area (2,360 m^2/g) and pore volume (1.98 cm^3/g), as well as hierarchical micro-/meso-/macropore structures resulting from nanosphere packing/aggregation. A-CNS21 shows outstanding high-rate supercapacitive performances, and sorption performances towards the storage of CO_2/H_2 and the capture of VOCs. It shows very high specific capacitance (305 F/g at 0.1 A/g) and remarkably high capacitance retention (72% retention at 10 A/g), which are well comparable to the best results achieved in the literature and are much superior compared to AC-PDEB, the activated carbon control sample. A-CNS21 also shows superior maximum adsorption capacities towards toluene and methanol vapors (967 and 937 mg/g, respectively, at P/P_0 of 0.99). Among various high-performance adsorbents reported to date, it shows the highest adsorption capacities towards the two VOCs at low concentrations (866 and 366 mg/g, respectively, at P/P_0 of 0.1). In addition, A-

CNS21 is also featured with high CO_2 (1 bar and 0 °C) and H_2 (1 bar and –196 °C) adsorption capacities (26 and 2.5 wt%, respectively). Given the high efficiency and easy scalability of the emulsion polymerization technique with the use of all commercially available precursors as well as the outstanding performances of the resulting carbon nanospheres, we expect the potential applications of this novel technique for large-scale tailored synthesis of well-defined ultra-small carbon nanospheres.

Acknowledgements

This work was financially supported by the grants from Canada Research Chair (Grant # 220084 and 230723) and the Natural Science and Engineering Research Council of Canada (Grant # RGPIN-2015-03815 and 477901-2015).

Notes and references

1 (a) J. Liu, N. P. Wickramaratne, S. Z. Qiao, M. Jaroniec, *Nature Mater.,* 2015, **14,** 763–774; (b) P. Zhang, Z.-A. Qiao, S. Dai, *Chem. Commun.,* 2015, **51,** 9246–9256; (c) A. D. Roberts, X. Li, H. Zhang, *Chem. Soc. Rev.*, 2014, **43,** 4341–4356; (d) A. Nieto-Márquez, R. Romero, A. Romero, J. L. Valverde, *J. Mater. Chem.,* 2011, **21**, 1664–1672.

2 (a) J. Lee, J. Kim, T. Hyeon, *Adv. Mater.,* 2006, **18**, 2073–2094; (b) H. Nishihara, T. Kyotani, *Adv. Mater.*, 2012, **24**, 4473–4498; (c) Y. Xia, Z. Yang, R. Mokaya, *Nanoscale*, 2010, **2**, 639–659; (d) B. Fang, J. H. Kim, M.-S. Kim, J.-S. Yu, *Acc. Chem. Res.,* 2013, **46**,1397–1406; (e) M. Antonietti, N. Fechler, T.-P. Fellinger, *Chem. Mater.*, 2014, **26**, 196–210; (f) Y. Zhai, Y. Dou, D. Zhao, P. F. Fulvio, R. T. Mayes, S. Dai, *Adv. Mater.,* 2011, **23**, 4828–4850.

3 Representative papers on effects of micropores on electrocapacitive energy storage: (a) J. Chmiola, G. Yushin, Y. Gogotsi, C. Portet, P. Simon, P. L. Taberna, *Science*, 2006, **313**, 1760–1763; (b) C. Largeot, C. Portet, J. Chmiola, P.-L. Taberna, Y. Gogosti, P. Simon, *J. Am. Chem. Soc.,* 2008, **130**, 2730–2731; (c) J. Chmiola, C. Largeot, P.-L. Taberna, P. Simon, Y. Gogosti, *Angew. Chem. Int. Ed.,* 2008, **47**, 3392–3395.

4 Representative papers on effects of micropores on H_2/CO_2 storage: (a) Y. Gogotsi, R. K. Dash, G. Yushin, T. Yildirim, G. Laudisio, J. E. Fischer, *J. Am. Chem. Soc.,* 2005, **127**, 16006–16007; (b) G. Yushin, R. Dash, J. Jagiello, J. E. Fischer, Y. Gogotsi, *Adv. Funct. Mater.,* 2006, **16**, 2288–2293; (c) N. Texier-Mandoki, J. Dentzer, T. Piquero, S. Saadallah, P. David, C. Vix-Guterl, *Carbon,* 2004, **42**, 2735–2777; (d) V. Presser, J. McDonough, S.-H. Yeon, Y. Gogotsi, *Energy Environ. Sci.,* 2011, **4**, 3059–3066; (e) J. Silvestre-Alberto, A. Wahby, A. Sepúlveda-Escribano, M. Martínez-Escandell, K. Kaneko, F. Rodríguez-Reinoso, *Chem. Commun.*, 2011, **47**, 6840–6842; (f) N. P. Wickramaratne, M. Jaroniec, J. *Mater. Chem. A*, 2013, **1**, 112–116.

5 Representative examples on hard-templating strategy: (a) A. B. Fuertes, *J. Mater. Chem.,* 2003, **13**, 3085–3088; (b) T.-W. Kim, P.-W. Chung, I. I. Slowing, M. Tsunoda, E. S. Yeung, V. S.-Y. Lin, *Nano Lett.,* 2008, **8**, 3724–3727; (c) Z. Lei, N. Christov, L. L. Zhang, X. S. Zhao, *J. Mater. Chem.*, 2011, **21**, 2274–2281; (d) J. Schuster, G. He, B. Mandlmeier, T. Yim, K. T. Lee, T. Bein, L. F. Nazar, *Angew. Chem. Int. Ed.*, 2012, **51**, 3591–3595; (e) Z. Sun, Y. Liu, B. Li, J. Wei, M. Wang, Q. Yue, Y. Deng, S. Kaliaguine, D. Zhao, *ACS Nano*, 2013, **7**, 8706–8714; (f) Z.-A. Qiao, B. Guo, A. J. Binder, J. Chen, G.M. Veith, S. Dai, *Nano Lett.* 2013, **13**, 207–212.

6 Representative examples on self-assembly strategy: (a) Y. Fang, D. Gu, Y. Zou, Z. Wu, F. Li, R. Che, Y. Deng, B. Tu, D. Zhao, *Angew. Chem. Int. Ed.,* 2010, **49**, 7987–7991; (b) J. Liu, T. Yang, D.-W. Wang, G. Q. Lu, D. Zhao, S. Z. Qiao, *Nature Commun.*, 2013, **4**, 2798; (c) T. Yang, J. Liu, R. Zhou, Z. Chen, H. Xu, S. Z. Qiao, M. J. Monteiro, *J. Mater. Chem. A,* 2014, **2**, 18139–18146; (d) J. Wang, H. Liu, J. Diao, X. Gu, H. Wang, J. Rong, B. Zong, D. S. Su, *J. Mater. Chem. A,* 2015, **3**, 2305–2313; (e) J. Tang, J. Liu, C. Li, Y. Li, M. O. Tade, S. Dai, Y. Yamauchi, *Angew. Chem. Int. Ed.*, 2015, **54**, 588–593; (f) A.-H. Lu, W.-C. Li, G.-P. Hao, B. Spliethoff, H.-J. Bongard, B. B. Schaack, F. Schüth, *Angew. Chem. Int. Ed.*, 2010, **49**, 1615–1618; (g) S. Wang, W.-C. Li, G.-P. Hao, Y. Hao, Q. Sun, X.-Q. Zhang, A.-H. Lu, *J. Am. Chem. Soc.,* 2011, **133**, 15304–15307; (h) S. Wang, W.-C. Li, L. Zhang, Z.-Y. Jin, A.-H. Lu, *J. Mater. Chem. A*, 2014, **2**, 4406–4412; (i) F. Xu, Z. Tang, S. Huang, L. Chen, Y. Liang, W. Mai, H. Zhong, R. Fu, D. Wu, *Nature Commun.,* 2015, **6**, 7221.

7 Representative examples on extended Stober strategy: (a) J. Liu, S. Z. Qiao, H. Liu, J. Chen, A. Orpe, D. Zhao, G. Q. Lu, *Angew. Chem. Int. Ed.*, 2011, **50**, 5947–5951; (b) J. Choma, D. Jamiola, K. Augustynek, M. Marszewski, M. Gao, M. Jaroniec, *J. Mater. Chem.* 2012, **22**, 12636–12642; (c) J. Ludwinowicz, M. Jaroniec, *Carbon*, 2015, **82**, 297–303; (d) N. P. Wickramaratne, M. Jaroniec, *ACS Appl. Mater. Interfaces* 2013, **5**, 1849–1855; (e) N. P. Wickramaratne, V. S. Perera, J. M. Ralph, S. D. Huang, M. Jaroniec, *Langmuir* 2013, **29**, 4032–4038; (f) J. Choma, W. Fahrenholz, D. Jamiola, J. Ludwinowicz, M. Jaroniec, *Microporous Mesoporous Mater.,* 2014, **185**, 197–203; (g) J. Qian, M. Liu, L. Gan, P. K. Tripathi, D. Zhu, Z. Xu, Z. Hao, L. Chen, D. S. Wright, *Chem. Commun.* 2013, **49**, 3043–3045; (h) X. Ma, L. Gan, M. Liu, P. K. Tripathi, Y. Zhao, Z. Xu, D. Zhu, L. Chen, *J. Mater. Chem. A,* 2014, **2**, 8407–8415; (i) J. Zhao, W. Niu, L. Zhang, H. Cai, M. Han, Y. Yuan, S. Majeed, S. Anjum, G. Xu, *Macromolecules,* 2013, **46**, 140–145; (j) Z. Xu, Q. Guo, *Carbon,* 2013, **52**, 464–467; (k) V. G. Pol, L. K. Shrestha, K. Ariga, *ACS Appl. Mater. Interfaces,* 2014, **6**, 10649–10655; (l) J. Wang, L. Yao, C. Ma, X. Guo, W. Qiao, L. Ling, D. Long, *ACS Appl. Mater. Interfaces,* 2016, **8**, 4851–4861; (m) K. Ai, Y. Liu, C. Ruan, L. Lu, G. Lu, *Adv. Mater.,* 2013, **25**, 998–1003.

8 Representative examples on hydrothermal carbonization strategy: (a) B. Hu, K. Wang, L. Wu, S.-H. Yu, M. Antonietti, M.-M. Titirici, *Adv. Mater.,* 2010, **22**, 813–828; (b) X. Sun, Y. Li, *Angew. Chem. Int. Ed.*, 2004, **43**, 597–601; (c) Y. Shin, L.-Q. Wang, I.-T. Bae, B. W. Arey, G. J. Exarhos, *J. Phys. Chem. C,* 2008, **112**, 14236–14240; (d) N. Baccile, M. Antonietti, M.-M. Titirici, *ChemSusChem*, 2010, **3**, 246–253; (e) T.-P. Fellinger, R. J. White, M.-M. Titirici, M. Antonietti, *Adv. Funct. Mater.,* 2012, **22**, 3254–3260; (f) P. Zhang, J. Yuan, T.-P. Fellinger, M. Antonietti, H. Li, Y. Wang, *Angew. Chem. Int. Ed.*, 2013, **52**, 6028–6032; (g) Y. Gong, Z. Wei, J. Wang, P. Zhang, H. Li, Y. Wang, *Sci. Rep.,* 2014, **4**, 6349.

9 Representative examples on emulsion polymerization strategy: (a) J. Jang, H. Yoon, *Small*, 2005, **1**, 1195–1199; (b) W.-K. Oh, H. Yoon, J. Jang, *Biomaterials*, 2010, **31**, 1342–1348; (c) S. Lee, K.-Y. Shin, J. Jang, *Nanoscale*, 2015, **7**, 9646–9654; (d) Y. Ouyang, H. Shi, R. Fu, D. Wu, *Sci. Rep.,* 2013, **3**, 1430; (e) F. Xu, R. Cai, Q. Zeng, C. Zou, D. Wu, F. Li, X. Lu, Y. Liang, R. Fu, *J. Mater. Chem.,* 2011, **21**, 1970–1976.

10 (a) S. Tanaka, H. Nakao, T. Mukai, Y. Katayama, Y. Miyake, *J. Phys. Chem. C*, 2012, **116**, 26791–26799; (b) X. Huang, S. Kim, M. S. Heo, J. E. Kim, H. Suh, I. Kim, *Langmuir*, 2013, **29**, 12266–12274; (c) B. Chang, Y. Guo, Y. Li, H. Yin, S. Zhang, B. Yang, X. Dong, *J. Mater. Chem. A*, 2015, **3**, 9565–9577.

11 (a) C. Portet, G. Yushin, Y. Gogotsi, *J. Electrochem. Soc.,* 2008, **155**, A531–A536; (b) C. R. Pérez, S.-H. Yeon, J. Ségalini, V. Presser, P.-L. Taberna, P. Simon, Y. Gogotsi, *Adv. Funct. Mater.,* 2013, **23**, 1081–1089.
12 S. Y. Lim, W. Shen, Z. Gao, *Chem. Soc. Rev.*, 2015, **44**, 362–381.
13 M. Grundy, Z. Ye, *J. Mater. Chem. A,* 2014, **2**, 20316–20330.
14 (a) Z. Dong, Z. Ye, *Macromolecules,* 2012, **45**, 5020–5031; (b) Z. Dong, Z. Ye, *Adv. Synth. Catal.,* 2014, **356**, 3401–3414; (c) Z. Dong, Z. Ye, *Appl. Catal. A: Gen.,* 2015, **489**, 61–71.
15 J. Huber, S. Mecking, *Macromolecules,* 2010, **43**, 8718–8723.
16 S.S. Sakhawat, Ejaz-ur-Rehman, Effect of temperature and aprotic solvents on the CMC of sodium dodecyl sulphate. in Interactions of Water in Ionic and Nonionic Hydrates (Ed. Kleeberg, H.) Springer-Verlag Berlin Heidelberg 1987, pp. 251–255.
17 K. S. W. Sing, D. H. Everett, R. A. W. Haul, L. Moscou, R. A. Pierotti, J. Rouquérol, T. Siemieniewska, *Pure Appl. Chem.,* 1985, **57**, 603–619.
18 L. Xu, J.-W. McGraw, F. Gao, M. Grundy, Z. Ye, Z. Gu, J. L. Shepherd, *J. Phys. Chem. C*, 2013, **117**, 10730–10742.
19 (a) Q. Zhao, T.-P. Fellinger, M. Antonietti, J. Yuan, *J. Mater. Chem. A*, 2013, **1**, 5113–5120; (b) D. Puthusseri, V. Aravindan, S. Madhavi, S. Ogale, *Energy Environ. Sci.,* 2004, **7**, 728–735.
20 L. Xu, L. Huang, Z. Ye, N. Meng, Y. Shu, Z. Gu, *Macromol. Rapid Commun.* 2017, **3**, 1600608.
21 T. Ben, H. Ren, S. Ma, D. Cao, J. Lan, X. Jing, W. Wang, J. Xu, F. Deng, J. M. Simmons, S. Qiu, G. Zhu, *Angew. Chem. Int. Ed.*, 2009, **48**, 9457–9460.
22 F. Xu, S. Xian, Q. Xia, Y. Li, Z. Li, *Adsorp. Sci. Tech.,* 2013, **31**, 325–339.
23 A. Wahby, J. M. Ramos-Fernández, M. Martínez-Escandell, A. Sepúlveda-Escribano, J. Silvestre-Albero, F. Rodríguez-Reinoso, *ChemSusChem,* 2010, **3**, 974–981.
24 S. J. Yang, T. Kim, J. H. Im, Y. S. Kim, K. Lee, H. Jung, C. R. Park, *Chem. Mater.*, 2012, **24**, 464–470.